Mon. Not. R. Astron. Soc. **388,** 56–66 (2008) doi:10.1111/j.1365-2966.2008.13391.x

Unresolved emission and ionized gas in the bulge of M31

Á. Bogdán[1]★ and M. Gilfanov[1,2]★

[1]*Max-Planck-Institut für Astrophysik, Karl-Schwarzschild-Str 1, 85741 Garching bei München, Germany*
[2]*Space Research Institute, Russian Academy of Sciences, Profsoyuznaya 84/32, 117997 Moscow, Russia*

Accepted 2008 April 25. Received 2008 April 15; in original form 2008 March 1

ABSTRACT

We study the origin of unresolved X-ray emission from the bulge of M31 based on archival *Chandra* and *XMM–Newton* observations. We demonstrate that three different components are present. (i) Broad-band emission from a large number of faint sources – mainly accreting white dwarfs and active binaries, associated with the old stellar population, similar to the Galactic ridge X-ray emission of the Milky Way. The X-ray to *K*-band luminosity ratios are compatible with those for the Milky Way and for M32; in the 2–10 keV band, the ratio is $(3.6 \pm 0.2) \times 10^{27}$ erg s^{-1} $L_{\odot}^{-1}$. (ii) Soft emission from ionized gas with a temperature of about ∼300 eV and a mass of $\sim 2 \times 10^6$ $M_{\odot}$. The gas distribution is significantly extended along the minor axis of the galaxy, suggesting that it may be outflowing in the direction perpendicular to the galactic disc. The mass and energy supply from evolved stars and Type Ia supernovae is sufficient to sustain the outflow. We also detect a shadow cast on the gas emission by spiral arms and the 10-kpc star-forming ring, confirming significant extent of the gas in the 'vertical' direction. (iii) Hard extended emission from spiral arms, most likely associated with young stellar objects and young stars located in the star-forming regions. The L_X/SFR (star formation rate) ratio equals $\sim 9 \times 10^{38}$ (erg s^{-1})($M_{\odot}$ yr^{-1})$^{-1}$, which is about ∼1/3 of the high-mass X-ray binary contribution, determined earlier from *Chandra* observations of other nearby galaxies.

Key words: ISM: general – galaxies: individual: M31 – galaxies: stellar content – X-rays: diffuse background – X-rays: galaxies.

1 INTRODUCTION

The X-ray radiation from the majority of galaxies is dominated by X-ray binaries (e.g. Fabbiano 2006). In addition, extended emission is present in galaxies of all morphological types. At least part of this emission is associated with the stellar population and is a superposition of a large number of faint compact sources – accreting white dwarfs, active binaries and other types of stellar sources, old and young (Revnivtsev et al. 2006; Sazonov et al. 2006). There is also a truly diffuse component – emission from ionized gas of sub-keV temperature. Its importance varies from galaxy to galaxy, with luminous gas-rich ellipticals like NGC 1316 (Kim & Fabbiano 2003) and dwarf galaxies similar to M32 (Revnivtsev et al. 2007) representing the two opposite ends of the range. Significant diffuse or quasi-diffuse emission is also associated with star formation, the Antennae (e.g. Baldi et al. 2006) being one of the nearby examples. The morphology of the gas in starburst galaxies often indicates outflows, driven by the energy input into the interstellar medium (ISM) from core-collapse supernovae. Theoretical considerations suggest that gas in low-mass elliptical galaxies may also be in the state of outflow (David et al. 2006). The mass and energy budget of the ISM in this case is maintained by winds from evolved stars and Type Ia supernovae. The overall X-ray radiation from a galaxy is a superposition of these (and possibly other) components, their relative importance being defined by the morphological type of the galaxy and its star formation and merger history.

Our close-by neighbour, the M31 galaxy, gives a unique opportunity to explore a 'full-size' spiral galaxy similar to the Milky Way without complications brought about by projection and absorption effects, often hampering studies of our own Galaxy. Not surprisingly, it has been extensively investigated by every major observatory of the past decades. Observations by the *Einstein* observatory demonstrated that X-ray binaries account for the most of the X-ray emission from the galaxy (van Speybroeck et al. 1979; Fabbiano, Trinchieri & van Speybroeck 1987). Using the complete set of *Einstein* data, Trinchieri & Fabbiano (1991) constrained the possible amount of ionized gas in the bulge of the galaxy by $\lesssim 2 \times 10^6$ $M_{\odot}$. Based on the *ROSAT* observations, Primini, Forman & Jones (1993) found evidence for an extended emission component with a luminosity of $\sim 6 \times 10^{38}$ erg s^{-1} in the 0.2–4 keV band. They suggested that this emission may be of truly diffuse origin or due to a new class of X-ray sources. The unresolved emission from

★E-mail: bogdan@mpa-garching.mpg.de (ÁB); gilfanov@mpa-garching.mpg.de (MG)

M31 was investigated further by Supper et al. (1997), West, Barber & Folgheraiter (1997), Irwin & Bregman (1999) and Borozdin & Priedhorsky (2000). In all these studies, the existence of a soft emission component with temperature $kT \sim 0.3$–0.4 keV has been confirmed, although different authors suggested different explanations of its origin. With the advent of *Chandra* and *XMM–Newton*, the consensus seemed to be achieved in favour of a truly diffuse origin of the soft emission component (Shirey et al. 2001; Takahashi et al. 2004). However, recent progress in understanding the nature of the Galactic ridge emission as a superposition of a large number of faint stellar type sources (Revnivtsev et al. 2006) made it worth revisiting the problem of the origin of extended emission in M31. Also, with more *Chandra* and *XMM–Newton* observations, more accurate and detailed investigations became possible. Recently, Li & Wang (2007) analysed a large *Chandra* data set of M31 bulge observations and demonstrated the presence of both ionized gas and emission of faint compact sources associated with the old stellar population. Moreover, they revealed a peculiar morphology of the gas emission and suggested that the X-ray gas in the bulge of M31 may be in the state of outflow.

In the present paper, we combine an extensive set of *Chandra* and *XMM–Newton* observations to obtain a broad band and large field view of the X-ray emission originating in and around the bulge of M31. We restrict our study to the central region of ∼20 arcmin in radius, covered well by *Chandra* and *XMM–Newton* observations currently available in the public archives of these observatories (Fig. 1). The investigated region has a linear size of ∼4 kpc along the major axis of the galaxy, but extends out to ∼16 kpc along the plane of the galaxy in the minor axis direction, due to the rather large inclination angle of M31, $i \sim 77^\circ$ (Henderson 1979). We assume the distance to Andromeda of 780 kpc (Stanek & Garnavich 1998; Macri et al. 2001). The Galactic absorption towards M31 is 6.7×10^{20} cm^{-2} (Dickey & Lockman 1990).

This paper is structured as follows. In Section 2, we describe the data and their reduction. We introduce our results in Section 3, where we present the spatial distribution, the morphology and the spectra of the extended emission. In Section 4, the origin, properties and physical parameters of different components are discussed and in Section 5 we summarize our results.

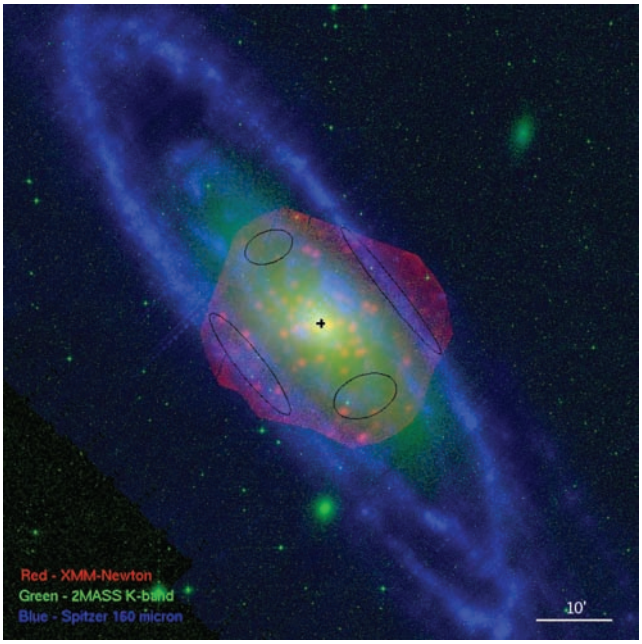

Figure 1. RGB image of M31. The colours are as follows: red denotes the *XMM–Newton* data in the 0.5–1.2 keV band, green is an image of the *K*-band light from 2MASS and blue is the 160 μm image of *Spitzer*. The centre of M31 is marked with a cross. North is up and east is left.

Table 1. The list of *Chandra* observations used for the analysis.

Obs-ID	$T_{\rm original}$	$T_{\rm eff}$	Instrument	Date
303	12.0 (ks)	8.2 (ks)	ACIS-I	1999 Oct 13
305	4.2 (ks)	4.0 (ks)	ACIS-I	1999 Dec 11
306	4.2 (ks)	4.1 (ks)	ACIS-I	1999 Dec 27
307	4.2 (ks)	3.1 (ks)	ACIS-I	2000 Jan 29
308	4.1 (ks)	3.7 (ks)	ACIS-I	2000 Feb 16
311	5.0 (ks)	3.9 (ks)	ACIS-I	2000 Jul 29
312	4.7 (ks)	3.8 (ks)	ACIS-I	2000 Aug 27
1575	38.2 (ks)	38.2 (ks)	ACIS-S	2001 Oct 05
1577	5.0 (ks)	4.9 (ks)	ACIS-I	2001 Aug 31
1583	5.0 (ks)	4.1 (ks)	ACIS-I	2001 Jun 10
1585	5.0 (ks)	4.1 (ks)	ACIS-I	2001 Nov 19
2895	4.9 (ks)	3.2 (ks)	ACIS-I	2001 Dec 07
2896	5.0 (ks)	3.7 (ks)	ACIS-I	2002 Feb 06
2897	5.0 (ks)	4.1 (ks)	ACIS-I	2002 Jan 08
2898	5.0 (ks)	3.2 (ks)	ACIS-I	2002 Jun 02
4360	5.0 (ks)	3.4 (ks)	ACIS-I	2002 Aug 11
4678	4.9 (ks)	2.7 (ks)	ACIS-I	2003 Nov 09
4679	4.8 (ks)	2.7 (ks)	ACIS-I	2003 Nov 26
4680	5.2 (ks)	3.2 (ks)	ACIS-I	2003 Dec 27
4681	5.1 (ks)	3.3 (ks)	ACIS-I	2004 Jan 31
4682	4.9 (ks)	1.2 (ks)	ACIS-I	2004 May 23

2 DATA REDUCTION

We combine data from the *Chandra* and *XMM–Newton* satellites, adding their benefits together. The primary advantage of *Chandra* is its good angular resolution which allows us to resolve individual X-ray binaries everywhere including the very central region of the bulge. *XMM–Newton* provided better coverage of M31 and collected more photons, thanks to its larger effective area. It is more suitable to study the outer part of M31. On the other hand, the higher and less predictable background of *XMM–Newton* complicates the study of low surface brightness regions.

2.1 *Chandra*

We used 21 archival *Chandra* observations listed in Table 1, taken between 1999 October 13 and 2004 May 23. For the analysis, we extracted data of the ACIS-I array except for Obs-ID 1575 where we used only the S3 chip. The pattern of available *Chandra* observations allows us to study the central ≈15 arcmin region. The data reduction was performed using standard CIAO[1] software package tools (CIAO version 3.4; CALDB version 3.4.1). For each observation, we filtered out the flare-contaminated intervals, excluding the time intervals where the count rate deviated by more than 20 per cent from the mean value. The resulting effective exposure times are given in Table 1.

Crucial for the analysis of the low surface brightness outer regions is the accuracy of the background subtraction. In treating the *Chandra* background, we generally followed the procedures outlined

[1] http://cxc.harvard.edu/ciao/

in Hickox & Markevitch (2006). We determined the level of the instrumental background using the stowed data set.[2] In the stowed position of ACIS detectors, the sky emission is blocked and only the instrumental background gives a contribution. As demonstrated in the above-mentioned paper, although the instrumental background level varies with time, its spectrum remains unchanged. The effective area of *Chandra* is negligible above 9 keV and the count rate is dominated by the instrumental background. Therefore, the 9.5–12 keV count rates can be used to renormalize background spectra obtained from the stowed data sets. In dealing with cosmic background, we took into account that it consists of the soft emission associated with the Galaxy and a harder extragalactic component, and treated them separately. For the soft Galactic component, we used the best-fitting spectrum from Hickox & Markevitch (2006). For the extragalactic background, we took into account that some fraction of it has been resolved in our data analysis procedure and removed along with X-ray binaries. Using the incompleteness function from Voss & Gilfanov (2007), which was obtained using essentially the same data set, we estimated that our point source detection sensitivity in the outer regions is $\approx 5 \times 10^{35}$ erg s^{-1}. We used the sensitivity for the outermost regions because the cosmic X-ray background (CXB) subtraction plays role only in these regions where the surface brightness of the source emission is low. This point source sensitivity results in the resolved CXB fraction of ≈50 per cent, according to Moretti et al. (2003). The Galactic and cosmic backgrounds were subtracted from the vignetting-corrected images and profiles.

In order to study the diffuse emission we need to exclude the contribution of bright low-mass X-ray binaries. According to the luminosity functions of low-mass X-ray binaries and faint compact sources associated with the old population (Gilfanov 2004; Sazonov et al. 2006), the contribution of the former is defined by the sources more luminous than $\log L_X \sim 35.5$–36.0. Below this threshold, active binaries and cataclysmic variables are the dominating X-ray sources. The individual *Chandra* observations are too short (typically, ∼4 ks; see Table 1) to achieve this sensitivity, therefore we ran point source detection on the combined image with a total exposure of $T_{\rm eff} = 112.6$ ks. To combine the data, each observation was projected into the coordinate system of Obs-ID 303 and the attitude corrections from Voss & Gilfanov (2007) were applied in order to better co-align individual event lists. To detect point sources, we ran the CIAO WAVDETECT tool in the 0.5–8 keV band. Some parameters were changed from the default values to fit our aims. The scales on which we were looking for sources were the $\sqrt{2}$-series from 1.0 to 8.0. To minimize the contribution of residual counts from point sources to diffuse emission, we increased the value of the sigma parameter to 4; this parameter describes the size of elliptical source detection regions in standard deviations assuming a 2D Gaussian distribution of source counts. With these adjustments, we obtained larger source regions than usual, including a larger fraction of source counts. To increase sensitivity, we did not filter out flare containing time intervals for point source detection. The resulting source list consisted in total of 238 sources in the investigated area; the detected sources are in good agreement with the results of Voss & Gilfanov (2007). The sensitivity limit in the central region was 10^{35} erg s^{-1}, while in the outermost region it deteriorated to 5×10^{35} erg s^{-1}. Extracting the point spread function (PSF) with MKPSF for each source, we calculated the fraction of counts inside the source cell. For most of the sources, this fraction exceeded 98 per cent; if it was smaller then the source cells were enlarged accordingly. The output source cells were used to mask out the point sources for further image and spectral analysis.

[2] http://cxc.harvard.edu/contrib/maxim/stowed/

Table 2. The list of *XMM–Newton* observations used for the analysis.

Obs-ID	$T_{\rm original}$	$T_{\rm eff}$	Date
0109270101	62.5 (ks)	16.0 (ks)	2001 Jun 29
0112570101	61.1 (ks)	52.6 (ks)	2002 Jan 6
0112570401	31.0 (ks)	25.0 (ks)	2000 Jun 25
0202230201	18.3 (ks)	17.8 (ks)	2004 Jul 16
0202230401	14.6 (ks)	9.0 (ks)	2004 Jul 18
0202230501	21.8 (ks)	2.0 (ks)	2004 Jul 19

We produced exposure maps using a two-component spectral model consisting of an optically thin thermal plasma emission with a temperature of 0.30 keV and a power-law component with a slope of $\Gamma = 1.80$. The ratio of the normalizations of these two components was 3/1. This is the best-fitting two-component model to the spectrum of the central 200 arcsec region.

2.2 *XMM–Newton*

We analysed six archival *XMM–Newton* observations taken between 2000 June 25 and 2004 July 19, as listed in Table 2. We used the data of the European Photon Imaging Camera (EPIC) instruments (Strüder et al. 2001; Turner et al. 2001). For data reduction, we used Science Analysis System (SAS) version 7.1.

In order to exclude the flare-contaminated time intervals, we double filtered the light curves using hard-band ($E > 10$ keV) and soft-band ($E = 1$–5 keV) energy ranges according to Nevalainen, Markevitch & Lumb (2005), using 20 per cent threshold for deviation from the mean count rate. The remaining useful exposure time is about 58 per cent of the original value. The data were cleaned from the out of time events using the Oot event lists.

The observations were re-projected into the coordinate system of Obs-ID 0112570101 and merged together. For point source removal, we combined the source list obtained from *Chandra* and *XMM–Newton* observations. In regions which lay outside the field of view of *Chandra*, we ran the SAS source detection task to complement the *Chandra* source list. The source regions were enlarged to account for the larger size of the PSF of *XMM–Newton* mirrors; their size was adjusted to approximately match the ∼90–98 per cent PSF-encircled energy radius depending on the brightness of the point source. It was not possible to reliably exclude the point source contribution in the crowded central ∼100 arcsec region, therefore it was not used in the following analysis. Exposure maps were calculated using the EEXPMAP command of SAS. In transforming the counts to flux units, we assumed the same spectrum as for *Chandra*.

The particle background on EPIC CCDs consists of two components. The 'internal' component is generated in interactions of cosmic rays with the detector material and is approximately uniform across the detector. The second component is due to low-energy solar protons, concentrated by the mirror systems of the telescopes; it is vignetted by the mirrors' response but the vignetting is flatter than that for photons. The level of both background components is variable (see http://www.star.le.ac.uk/∼amr30/BG/BGTable.html for details). According to this, we performed the background subtraction in two steps. At the first step, the corners of the CCDs which lie outside of the field of view were used to determine the level of the flat internal background. The obtained background level was subtracted from each observation individually. The combined

contribution of the solar proton component and cosmic background was approximately determined from the observations of nearby fields without extended sources and was subtracted from the final vignetting-corrected image. This method is not perfect, due to the difference in the shape of the vignetting function between solar protons and photon and due to variability of the solar proton level. However, good agreement between emission spectra obtained from *Chandra* and *XMM–Newton* data confirms the adequate accuracy of this procedure.

3 RESULTS

3.1 Images

The RGB image in Fig. 1 presents the *XMM–Newton* data (red) overlaid on the 160 μm *Spitzer* image (Rieke et al. 2004) (blue) and the *K*-band image from the Two-Micron All Sky Survey (2MASS) Large Galaxy Atlas (Jarrett et al. 2003) (green). Although the main purpose of this image is to show the X-ray data coverage, it crudely illustrates the presence of a large population of compact sources as well as of the extended emission. It also demonstrates the effect of the spiral arms on X-ray surface brightness distribution.

The brightness distribution of the extended emission, after the removal of the point sources, is shown in Fig. 2 along with the contours of the *K*-band brightness. The X-ray image was constructed from *Chandra* data in the 0.5–1.2 keV band. The point sources were excluded and their locations were filled up with the average local background around the sources. The X-ray image is adaptively smoothed. In order to compare the X-ray surface brightness with the distribution of the stellar mass, we also show *K*-band contours. The surface brightness of the extended emission approximately follows the *K*-band distribution but the image suggests that the agreement is not perfect and some distortions in the east–west direction may be present. In order to investigate this in detail, we consider profiles along the major and minor axes of the galaxy.

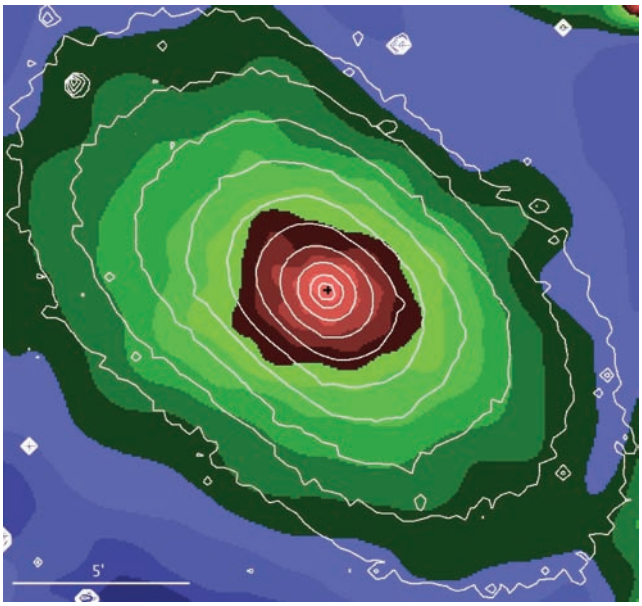

Figure 2. Adaptively smoothed *Chandra* image in the 0.5–1.2 keV band overplotted with *K*-band contours. The point sources were removed and their locations were filled with the local background value. The centre of M31 is marked with a cross. North is up and east is left.

3.2 Surface brightness distribution along the major and minor axes

We studied the brightness distribution in two energy bands, 0.5–1.2 and 2–7 keV. Our choice had been motivated by the shape of the spectrum of extended emission discussed in the next section. The profiles were constructed along the major and minor axes with position angles of 45° and 135°, respectively. For each profile, surface brightness was averaged over 500 arcsec in the transverse direction, corrected for vignetting and the estimated background level was subtracted. For *XMM–Newton*, the background level was adjusted to achieve better agreement with *Chandra* profiles. The adjusted values were well within the range of the background levels observed in individual blank-sky observations and differed from the average blank-sky level by $\lesssim 20$ per cent. The values of background were $(4.3, 5.6, 5.2, 6.2) \times 10^{-19}$ erg s^{-1} arcsec^{-2} cm^{-2} for *Chandra* (soft, hard) and *XMM–Newton* (soft, hard), respectively. For all distributions, we found good agreement between the *Chandra* and *XMM–Newton* data. We compare the X-ray distribution with profiles of the *K*-band emission. As is well known, the latter is a good stellar mass tracer. The *K*-band profile was obtained for the same regions as the X-ray profiles, in particular the same source regions were excluded in computing all profiles. The normalizations for the *K*-band profile are 4×10^{27} and 3×10^{27} erg s^{-1} $L_{\odot}^{-1}$ for soft and hard band, respectively.

In Fig. 3, we show the distribution along the major axis. In the 0.5–1.2 keV band, the profile shows an excess emission in the central

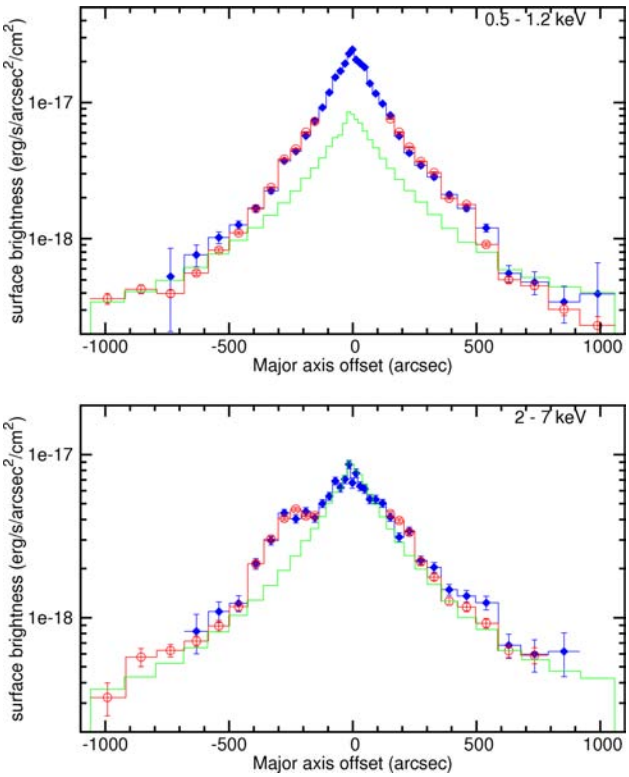

Figure 3. Surface brightness distribution along the major axis. in the 0.5–1.2 keV (upper panel) and 2–7 keV (lower panel) energy bands, background subtracted. The filled symbols (blue in the colour version of the plot) show the *Chandra* data, open symbols (red) show the *XMM–Newton* data and the solid histogram (green) without symbols is the normalized *K*-band brightness. The normalization factors are 4×10^{27} and 3×10^{27} erg s^{-1} $L_{\odot}^{-1}$ for soft and hard band, respectively. The *x*-coordinate increases from south-west to north-east.

part of the bulge. At bigger central distances, the X-ray and *K*-band light follow each other. In the hard band, the X-ray surface brightness follows the near-infrared light distribution rather well at all central distances, with the exception of the shoulder at the offset of −300 arcsec. The excess luminosity of the shoulder above the level suggested by the *K*-band profile is $\sim 2 \times 10^{37}$ erg s^{-1}. Its origin is unclear. There is not any easily identifiable feature in the image with which it could be associated. It cannot be due to residual contamination from point sources. Indeed, the excess count rate associated with the shoulder is ∼20 per cent of the total count rate of all point sources detected in this region. This is much larger than the expected residual contamination from point sources in *Chandra* images, $\lesssim$2–3 per cent. Good agreement between *Chandra* and *XMM–Newton* data also excludes the possibility that it is caused by an irregularity in the instrumental background.

The soft band profile along the minor axis (Fig. 4) at all offsets exceeds the level suggested by the *K*-band profile normalized according to the X/*K* ratio from the major axis distribution. Moreover, the X/*K* ratio increases significantly outside ∼500 arcsec from the centre – the X-ray distribution appears to have 'wings' extending out to ∼900 arcsec or more. Note that exact shape of the surface brightness distribution at large offsets from the centre depends on the adopted blank-sky level. The latter cannot be directly determined from the currently available data, due to its limited field of view. For this reason, we used the average CXB level and corrected it for the fraction of resolved background sources, as described in Section 2.1. The obtained value, $\sim$ (4–5) $\times 10^{-19}$ erg s^{-1} cm^{-2}, is comparable to the remaining (background subtracted) flux as can be seen in Fig. 4. Therefore, the extent of the X-ray emission at large off-centre angles cannot be unambiguously constrained from the present data. In order to eliminate this uncertainty, more extensive *Chandra* observations, including large offset angles, are needed. We note, however, that the existence of unresolved emission at large offsets is independently confirmed by the east–west asymmetry of the shadow cast by the 10-kpc star-forming ring, as discussed below.

There is a clear asymmetry between eastern and western halves of the profile, the latter being notably suppressed at offset values of +300 and +600 arcsec. The origin of this asymmetry becomes clear after comparison with the 160 μm *Spitzer* profile. The far-infrared profile, plotted in Fig. 4, shows several prominent peaks, corresponding to the 10-kpc star-forming ring and inner spiral arms (Gordon et al. 2006). The surface brightness suppressions in the western side of the profile (positive offsets) correspond to the spiral arm and the 10-kpc ring. On the other hand, no significant effect of the 10-kpc ring can be seen on the eastern side of the galaxy (negative offsets).

The spatial orientation of M31 plays an important role in understanding the link between the X-ray and far-infrared distributions. We see the galaxy with approximately 77° inclination (Henderson 1979) and the western side of the galactic disc is closer to us (Simien et al. 1978). The effect of this is that we see the western side of the bulge through the spiral arms, so the neutral gas and dust in the star-forming regions cast a shadow on the extended emission in the soft band. The eastern side of the disc, in contrast, is located behind the bulge and does not obscure its emission. We estimated the column density of the obscuring material in the spiral arms using the observed brightness difference between the eastern and western sides and obtained $N_{\rm H} \sim 1$–3×10^{21} cm^{-2}. These numbers are compatible with values derived from CO maps (Nieten et al. 2006).

In the hard band profile along the minor axis, we see correlation between the X-ray and far-infrared emission – the X-ray brightness appears to increase at the positions of spiral arms. This suggests that spiral arms are sources of harder X-ray emission. To further illustrate the impact of spiral arms on the observed X-ray brightness, we plot in Fig. 5 the hardness ratio along the minor axis together with the 160 μm distribution. This plot confirms the presence and significance of the soft emission in the centre. The hardness ratio has clear peaks at the positions of spiral arms, which are caused by two effects – obscuration by neutral and molecular gas and dust in

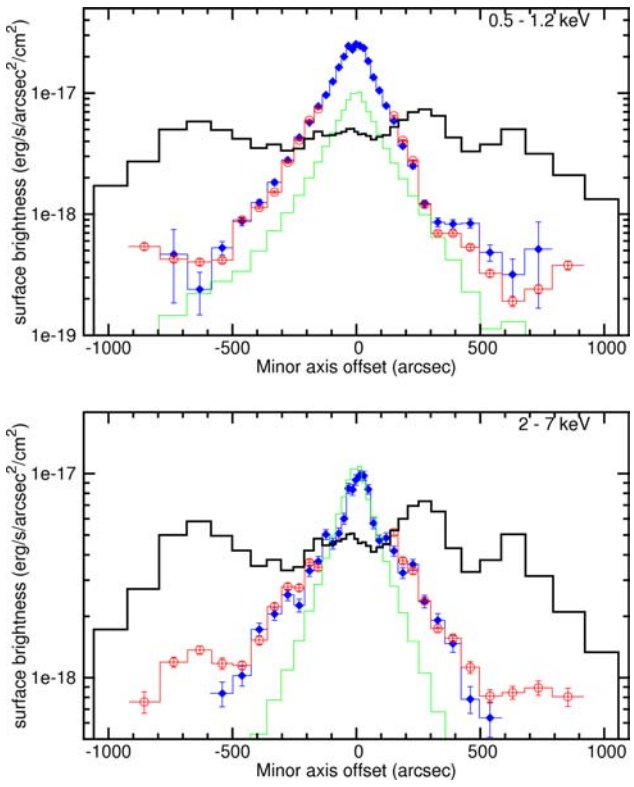

Figure 4. Same as Fig. 3 but along the minor axis. The normalizations of the *K*-band profile are the same as in Fig. 3. The solid histogram with multiple peaks (black) shows the distribution of the 160 μm emission as obtained by *Spitzer*. The *x*-coordinate increases from south-east to north-west.

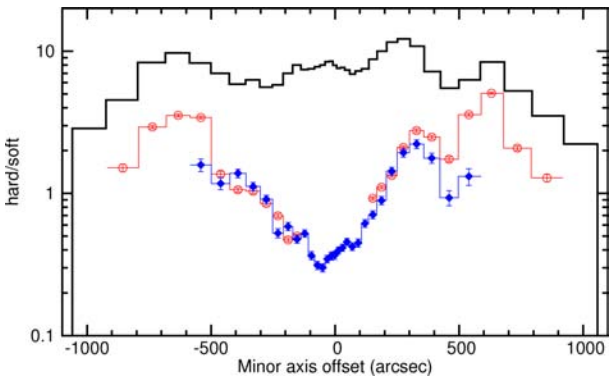

Figure 5. The X-ray hardness ratio profile along the minor axis, computed using the energy bands from Fig. 4. The *Chandra* and *XMM–Newton* data are presented by the same symbols as in Fig. 4. The solid histogram (black) shows the distribution of the 160 μm emission obtained by *Spitzer*. The *x*-coordinate increases from south-east to north-west.

the soft band and enhanced hard emission associated with the spiral arms.

Based on the X-ray brightness distributions, we conclude that there are at least three different components in the unresolved X-ray emission from the central region of M31:

(i) a broad-band component, following the distribution of *K*-band light (i.e. of stellar mass),

(ii) soft emission, localized in the central ∼500 arcsec along the major axis of the galaxy and extending out to ∼900 arcsec or more along the minor axis,

(iii) harder emission from the spiral arms and 10-kpc star-forming ring.

3.3 Spectra

We used the ACIS 'blank-sky' files in order to subtract the background from *Chandra* spectra. As before, we renormalized the background spectra using the 9.5–12 keV band count rates. For *XMM–Newton*, we used a combined spectrum of observations of nearby fields as a background spectrum and renormalized it using the 10–12 keV count rate. We found good agreement between *Chandra* and *XMM–Newton* spectra in all investigated regions.

In Fig. 6, we show spectra of different regions in M31. The spectral extraction regions are depicted in Fig. 1. The spectra of outer bulge and spiral arms are based on *XMM–Newton* data; other spectra are from *Chandra*. Also shown is the spectrum of M32. It was obtained using *Chandra* observations Obs-ID 2017, 2494 and 5690 with an exposure time of $T_{\rm eff} = 168.5$ ks. The spectrum was extracted from an elliptical region with a position angle of 40° and with 90 arcsec major and 71 arcsec minor axes; the data analysis procedures were identical to M31. All spectra are normalized to the same level of *K*-band brightness. The spectral fitting was done in the 0.5–7 keV band. The element abundances were fixed at the solar value and the hydrogen column density was fixed at the Galactic value. The results of spectral fits are summarized in Table 3.

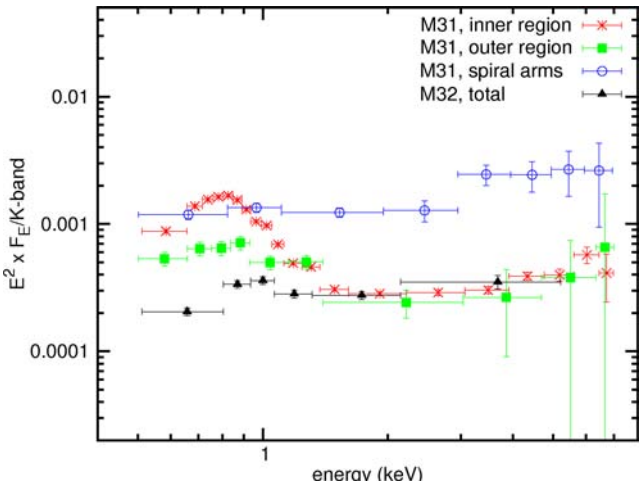

Figure 6. X-ray spectra of different regions in M31 and of M32: stars (red) – inner bulge – the spectrum of the central 200 arcsec region; filled boxes (green) – outer bulge – combined spectrum of two elliptical regions at ∼700 arcsec from the centre along the major axis; open circles (blue) – spiral arms – two elliptical regions at the 10-kpc ring; filled triangles (black) – spectrum of M32. The M31 regions are shown in Fig. 1. The inner bulge and M32 spectra are obtained by *Chandra* and outer bulge and spiral arms by *XMM–Newton*. All spectra are normalized to the *K*-band flux.

All spectra shown in Fig. 6 have a prominent power-law component with the photon index of approximately $\Gamma \sim 2$ and a soft component of varying strength. It is strongest in the inner bulge where it by far dominates X-ray emission below 1.2 keV. The best-fitting temperature of the soft component in the M31 spectra obtained in the two-component model is in the ∼0.3–0.4 keV range (Table 3). As can be seen from the table, the simple two-component model consisting of a power law and optically thin thermal plasma emission spectrum (MEKAL model in XSPEC) does not adequately describe the spectra, especially the spectrum of the inner bulge, having the largest number of counts. The deviations are due to the soft band, pointing at the complex shape of the soft component. With the second MEKAL component, the fit improves significantly: the best-fitting parameters for the inner bulge spectrum are $kT_1 \approx 0.2$ keV and $kT_2 \approx 0.5$ keV with $\chi^2 = 227$ for 184 d.o.f. Making the element abundance a free parameter improves the fit quality of the three-component model further to $\chi^2 = 205$ for 183 d.o.f. with the best-fitting abundance of 0.17 of the solar value. We considered several other spectral models with free element abundance; they all produced subsolar values in the range of 0.1–0.2. We also tried to vary element abundances individually and found that the model is most sensitive to Ne, Fe and Ni abundances with the best fit achieved when the abundances of Ni are a free parameter. The two-component (vmekal + power law) model requires a Ni abundance approximately three to four times the solar value (abundances of other elements were fixed at solar). In contrast, the models with the free Fe abundance give subsolar best-fitting values for the latter, ∼0.6. The fit quality improves further with the non-equilibrium thermal emission model (vnei model in XSPEC) with the best-fitting value of $n_{\rm e}\,t \sim 5 \times 10^{11}$ s cm^{-3} and a similar dependence on the element abundances as for vmekal model. All these modifications do not change the best-fitting temperature significantly. However, none of the models achieves acceptable values of χ^2. It is unclear how much weight should be given to these results, as they can be an artefact of the inadequate spectral model and insufficient energy resolution of the ACIS-I detector. Indeed, the emission from the inner bulge has a complex spectrum composed of several constituents of different temperature and ionization state, some of which may be out of the collisional ionization equilibrium.

The outer bulge spectrum has a less prominent soft component, approximately by a factor of 3 weaker than the inner bulge, but its temperature, $kT \approx 0.3$ keV, is compatible with the inner bulge value. The spectrum of M32 is similar, although only a very faint soft component is present here. Its temperature, $kT = 0.54 \pm 0.15$ keV, may be somewhat higher than in M31. All three spectra (inner and outer bulge in M31 and M32) nearly perfectly match each other above ∼1.2 keV, after normalization to the *K*-band flux. This is a strong argument in favour of their similar origin.

The emission from spiral arms clearly stands out. It does not have any significant soft component and, most importantly, its normalization (per unit *K*-band flux) is by a factor of 4–10 higher in the hard band than for the other spectra. This difference is smaller in the soft band, however it is still significantly higher than the spectrum of the outer region. We describe this spectrum with a power-law model and we obtain $\Gamma = 2.0$. As with other spectra, the large χ^2 value indicates a more complex spectral shape.

3.4 Morphology of the soft excess emission

To explore the spatial distribution of the soft excess emission, we use two approaches. First, we consider the ratio of the 0.5–1.2 keV X-ray image to the near-infrared image. The advantage of the ratio

Table 3. Results of the spectral fits in different regions of M31 using *Chandra* and *XMM–Newton* observations. PL denotes the power law and MKL is the optically thin thermal plasma emission model.

	Inner region		Outer region		Spiral arms		M32	
Model	Γ/kT	χ^2/(d.o.f.)	Γ/kT	χ^2/(d.o.f.)	Γ/kT	χ^2/(d.o.f.)	Γ/kT	χ^2/(d.o.f.)
PL	–	–	–	–	2.00 ± 0.15	292/192	2.07 ± 0.15	113/72
PL	1.79 ± 0.10		$2.48^{+0.55}_{-0.44}$				1.65 ± 0.21	
MKL	0.36 ± 0.01	312/186	0.31 ± 0.08	127/101	—	—	0.54 ± 0.15	83/70

image is that it levels out the component in X-ray emission which is proportional to the *K*-band light. The disadvantage is that the X/*K* ratio may become very large at large central distances, where the X-ray emission is unrelated to the old stellar population and deviates significantly from the *K*-band light distribution. Before producing the ratio image, we excluded point sources and filled their locations with the local background level using the DMFILTH tool of CIAO. The X-ray images were adaptively smoothed and the near-infrared image was convolved with a Gaussian with width comparable to the typical smoothing width near the centre of X-ray image. The X-ray images were exposure corrected, the particle background and CXB were subtracted.

Fig. 7 shows the ratio images obtained from *Chandra* and *XMM–Newton* data. They are consistent with each other and illustrate very well the morphology of the soft excess emission. Comparison with the *K*-band contours shown in the left-hand panel clearly demonstrates that the soft excess emission has nothing to do with the old stellar population traced by the near-infrared light. Unlike stellar light, it is strongly elongated in the approximate direction of the minor axis of the galaxy, extending beyond the boundaries of the bulge and projecting on to the 10-kpc star-forming ring. The images also reveal strong east–west asymmetry, already seen in the minor axis distribution (Fig. 4). As discussed in Section 3.2, this asymmetry is caused by absorption of soft X-rays by the neutral and molecular gas in the spiral arms on the north-western side of the galactic disc. This conclusion is further supported by the anti-correlation between the 160 μm flux and the soft X-ray brightness, with obvious shadows seen at the positions of spiral arms (Fig. 7, right-hand panel). At the same time, the gas and dust do not have any significant effect on the soft X-ray brightness in the south-eastern side of the galaxy.

In the second approach, we consider the difference between the X-ray and the *K*-band images, the latter renormalized according to the X/*K* ratio of the old stellar population component. Unlike the ratio image, it shows the true brightness distribution of the soft excess emission. For this purpose, we used the same 0.5–1.2 keV *Chandra* image as for the ratio image; the normalization of the *K*-band image was $4 \times 10^{27}\,\mathrm{erg\,s^{-1}\,L_\odot^{-1}}$. Fig. 8 shows the result. The image generally confirms the overall morphology of the soft emission revealed by the ratio image.

The images show significant substructures in the inner ∼100–150 arcsec with an angular scale of about 30 arcsec. The origin of these substructures is not clear, although some correlation with the position of the peaks on the 160 μm image suggests that at least some of them may be caused by absorption. These substructures may deserve a special study which is beyond the scope of this paper.

3.5 L_X/L_K ratios

We calculate ratios of X-ray to *K*-band luminosity for the same spatial regions as used for the spectral analysis, characterizing the inner and outer bulge and spiral arms. As suggested by the spectra, the natural boundary between the soft and hard energy bands is

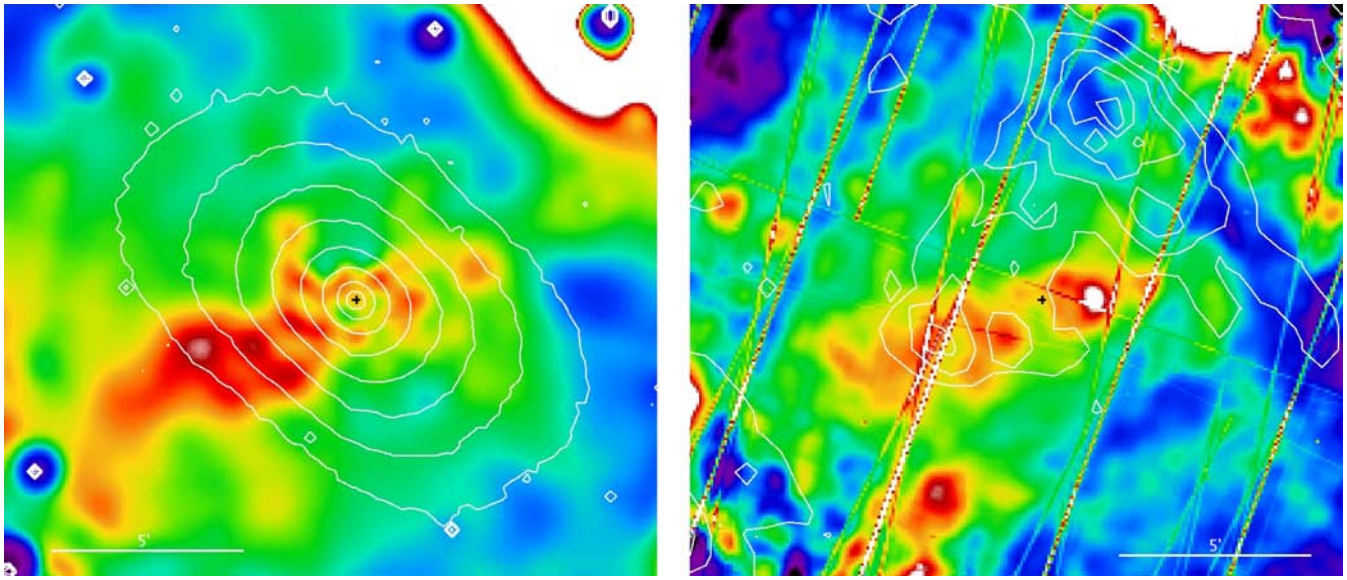

Figure 7. Ratio of the 0.5–1.2 keV image to the *K*-band image obtained from *Chandra* (left-hand panel) and *XMM–Newton* (right-hand panel) data. After the removal of the point sources, the X-ray images were adaptively smoothed; the *K*-band image was smoothed correspondingly. The contours in the left- and right-hand panels show *K*-band and 160 μm brightness distributions, respectively. The centre of M31 is marked with a cross. North is up and east is left.

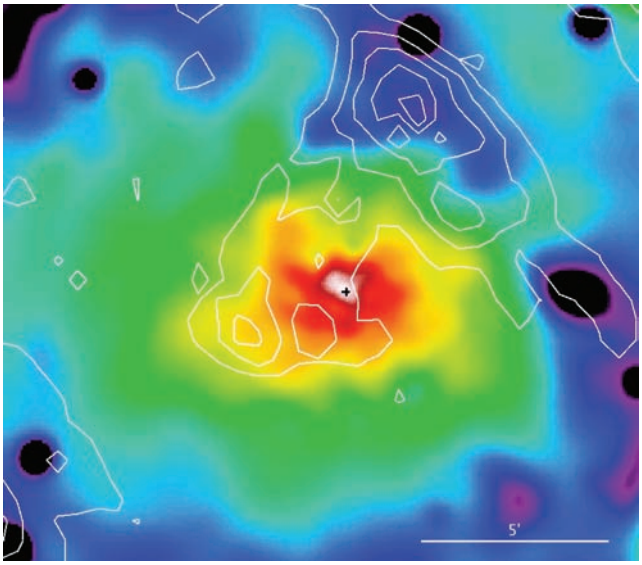

Figure 8. The spatial distribution of the soft component. The difference between the *Chandra* image in the 0.5–1.2 keV band and the *K*-band image normalized according to the X/*K* ratio of the outer bulge. The contours show the intensity levels of the 160 μm *Spitzer* image. The centre of M31 is marked with a cross. North is up and east is left.

1.2 keV. However, in order to facilitate a comparison with previous studies we computed the ratios in the 0.5–2 and 2–10 keV energy bands. The X-ray luminosities for these bands were computed using the best-fitting spectral models. The errors for the luminosity and, correspondingly, for X/*K* ratios account for the model normalization error only and do not include uncertainties in the spectral parameters or any other systematic uncertainties. In computing the hard band luminosity, we extrapolated the best-fitting model outside the energy range used for spectral fits, 0.5–7 keV. The *K*-band luminosities were calculated in each region using the 2MASS image.

The L_X/L_K ratios are presented in Table 4. These numbers can be transformed to X-ray-to-mass ratios dividing them with the *K*-band mass-to-light ratio, which is of the order of unity. Its value can be computed using the $B - V \approx 0.95$ colour index from Walterbos & Kennicutt (1987) and applying the relation between $M_\star/L_K$ and the $B - V$ colour (Bell & de Jong 2001), which gives $M_*/L_K \approx 0.85$. A close value has been derived by Kent (1992) based on the dynamical mass measurement, $M_*/L_K \approx 1.1$. We compare the X/*K* ratios for M31 with M32 and the Milky Way. The M32 numbers were obtained from the spectra of Section 3.3 in the same way as for M31. For the Milky Way, we used results from Revnivtsev et al. (2006) and Sazonov et al. (2006), and transformed them to L_X/L_K for two values of *K*-band mass-to-light ratio, 0.7 (Dwek et al. 1995) and 1 (Kent 1992). The X/*K* ratio in Sazonov et al. (2006) is given for the 0.1–2.4 keV band; following them we converted it to the 0.5–2 keV band multiplying by 0.7 which is a typical ratio for coronally active stars (Fleming et al. 1995). The contribution of young stars is excluded. Revnivtsev et al. (2006) used data from *RXTE* in the 3–20 keV band and calculated the 2–10 keV luminosities assuming a power-law spectrum with $\Gamma = 2.1$.

Table 4. X-ray to *K*-band luminosity ratios in different regions in M31 and in M32 compared to the Milky Way. All values are given in units of 10^{27} erg s^{-1} L$_\odot^{-1}$.

	0.5–2 keV[a]	2–10 keV
M31 inner bulge	9.4 ± 0.1	4.5 ± 0.1
M31 outer bulge	6.2 ± 0.1	3.6 ± 0.2
M31 spiral arms	22.1 ± 0.3	31.4 ± 0.6
M32 total	3.5 ± 0.1	4.1 ± 0.2
Galaxy (Sazonov et al. 2006)[b]	7.3–10.5(± 3)	2.2–3.1(± 0.8)
Galaxy (Revnivtsev et al. 2006)[b]	–	2.2–3.1(± 0.5)

[a]The X/*K* ratios for M31 and M32 were not corrected for absorption. See the text for the absorption-corrected values.
[b]The X/M_* ratios were converted to X/*K* ratios assuming two values of the *K*-band mass-to-light ratio, 0.7 (first number) and 1.0; the uncertainty given in the parentheses corresponds to $M_*/L_K = 1$.

In the 2–10 keV band, the X-ray to *K*-band ratios for bulge regions in M31 and for M32 are compatible with each other and appear to exceed slightly the Milky Way value. This may be explained by the difference in the spectral shape assumed in the flux calculation. Assuming the same power law with $\Gamma = 2.1$ as used by Revnivtsev et al. (2006), we obtained for M31 $L_X/L_K = (3.0 \pm 0.1) \times 10^{27}$ erg s^{-1} L$_\odot^{-1}$, in agreement with the Milky Way value. The good agreement of the X-ray to *K*-band ratios suggests a similar origin of the 2–10 keV emission in all three galaxies, as discussed in more detail in the following section.

In the soft band, the X/*K* ratios for M31 are systematically larger than M32 ones. This is to be expected from the spectra (Fig. 6) and is due to the presence of the soft excess emission in M31. Also, in interpreting the soft band ratios the interstellar absorption should be taken into account. Indeed, Sazonov et al. (2006) studied sources in the solar neighbourhood where the absorption is insignificant. The M31 and M32 data, in contrast, are subject to the Galactic absorption, with values of 6.7×10^{20} and 6.3×10^{20} cm^{-2}, respectively (Dickey & Lockman 1990). In addition, M31 has spatially variable internal absorption reaching a few $\times 10^{21}$ cm^{-2} in the spiral arm regions (Nieten et al. 2006). The total N_H for the outer bulge region in M31 is probably in the range (7–10) $\times 10^{20}$ cm^{-2}, giving the absorption-corrected value of the soft band X/*K* ratio $L_X/L_K \approx (8–10) \times 10^{27}$ erg s^{-1} L$_\odot^{-1}$. For M32, we obtain after absorption correction $L_X/L_K \approx 4.3 \times 10^{27}$ erg s^{-1} L$_\odot^{-1}$. Taking into account the uncertainties quoted by Sazonov et al. (2006) and uncertainties in the *K*-band mass-to-light ratio, the X/*K* ratio for the solar neighbourhood is formally compatible with the absorption-corrected value for M31 and probably slightly higher than for M32. It is unclear how much weight should be given to this discrepancy due to the number and amplitude of uncertainties involved. The absorption-corrected value for the inner bulge of M31 is definitely larger, $L_X/L_K \approx (12–15) \times 10^{27}$ erg s^{-1} L$_\odot^{-1}$.

The X/*K* ratios in the spiral arm region are significantly higher. The additional internal absorption can be up to a few $\times 10^{21}$ cm^{-2}, resulting in an absorption correction factor in the soft band as large as ≈4. The final X/*K* ratios in both bands are approximately an order of magnitude larger than for the Milky Way.

4 DISCUSSION

4.1 Faint compact sources

We showed that a broad-band emission component exists in M31 which (i) follows the *K*-band light distribution and (ii) has a 2–10 keV X/*K* ratio identical to that of M32 and the Milky Way. These suggest beyond reasonable doubt that this component has a similar origin to the Galactic ridge X-ray emission of the Milky Way (Revnivtsev et al. 2006). Namely, it is associated with the old stellar population and is a superposition of a large number of weak

sources of stellar type, the main contributors in the 2–10 keV band being cataclysmic variables and coronally active binaries (Sazonov et al. 2006).

The X/*K* ratios are compatible between all three galaxies in the 2–10 keV band, but in the soft band they differ in M31 and M32 (Table 4). In the inner bulge, this difference is clearly due to the contribution of the soft emission from the ionized gas, as discussed below. Although we chose the outer bulge region as far as possible along the major axis of the galaxy, where the soft X-ray brightness follows the *K*-band profile, some residual contribution from the gas cannot be entirely excluded. Therefore, it is not clear if this difference reflects a genuine difference between properties and/or content of X-ray emitting stellar populations in these two galaxies. Due to large systematic uncertainties, the Milky Way value is formally compatible with both galaxies and any quantitative comparison is inconclusive at this point.

4.2 Ionized gas

There are several arguments which suggest that the excess soft component has a non-stellar origin. The most important is the morphology of the excess emission, namely the striking difference from the distribution of the near-infrared light (Fig. 7). As no significant colour gradients are observed in the bulge of M31 (Walterbos & Kennicutt 1988), its stellar content must be sufficiently uniform and cannot give rise to the observed non-uniformities in the X/*K* ratio. An enhanced X-ray to *K*-band ratio could be explained if a notable young population was present in the bulge, which is also not the case (Stephens et al. 2003). With the stellar origin excluded, it is plausible that the soft excess emission is of truly diffuse nature and originates from ionized gas of ∼0.3–0.4 keV temperature.

To study the physical properties of the ionized gas, we use a rectangular region on the south-eastern side of the galaxy to avoid the complications due to attenuation by the spiral arms on the north-western side. The size of the region is 8 arcmin along the major axis and 10 arcmin along the minor axis of the galaxy. From the spectral fit, the total X-ray luminosity of the soft component in the 0.5–2 keV energy range is $\approx 10^{38}\,\mathrm{erg\,s^{-1}}$; after the absorption and bolometric correction the total bolometric luminosity is $L_{\rm bol} \approx 2.3 \times 10^{38}\,\mathrm{erg\,s^{-1}}$ assuming Galactic column density. From the emission measure of the gas, $\int n_{\rm e} n_{\rm H}\,{\rm d}V = 6.3 \times 10^{60}\,\mathrm{cm^{-3}}$, we estimate that the mass of the gas in the studied volume is of the order of $\sim 10^6\,\mathrm{M_\odot}$. We note that assuming the symmetry between the north-western and south-eastern sides of the galaxy, the total quantities for the mass and bolometric luminosity are twice the quoted values. The average number density is about $n_{\rm e} \sim 7 \times 10^{-3}\,\mathrm{cm^{-3}}$. The cooling time of the gas is $t_{\rm cool} = (3kT)/(n_{\rm e}\Lambda(T)) \sim 250$ million years. We also applied a two-temperature model to the soft emission and obtained for the two components: $kT_1 \sim 0.25$ keV, $kT_2 \sim 0.6$ keV, bolometric luminosities of $\sim 2 \times 10^{38}$ and $\sim 10^{38}\,\mathrm{erg\,s^{-1}}$, total masses of $\sim 10^6$ and $\sim 0.6 \times 10^6\,\mathrm{M_\odot}$ and cooling times of ∼200 and ∼800 million years. We mention that the above computed values strongly depend on the applied spectral model.

The morphology of the gas indicates that it is not in hydrostatic equilibrium in the gravitational potential of the galaxy. It suggests rather that gas is outflowing from the bulge in the direction perpendicular to the galactic disc (see also Li & Wang 2007). The mass and energy budget of the outflow can be maintained by the mass loss from the evolved stars and Type Ia supernovae. Knapp, Gunn & Wynn-Williams (1992) estimated the mass-loss rate from evolved stars for elliptical galaxies $\sim 0.0021\,L_K/\mathrm{L_{K,\odot}}\,\mathrm{M_\odot\,Gyr^{-1}}$. This rate can be applicable to the bulge of M31 as the stellar populations are similar. The *K*-band luminosity of this region is $L_K = 1.4 \times 10^{10}\,\mathrm{L_{K,\odot}}$. The estimated total mass-loss rate is $\approx 0.03\,\mathrm{M_\odot\,yr^{-1}}$. The stellar yields produce the total amount of observed gas on a time-scale of ∼35 million years which is shorter than the cooling time-scale of the gas.

To estimate the energy input from Type Ia supernovae, we use the results of Mannucci et al. (2005) who give the supernova rate of $N_{\rm SN\,Ia} = 0.035^{+0.013}_{-0.011}$ SNu for E and S0 galaxies, where $1\,\mathrm{SNu} = 1\,\mathrm{SN}/10^{10}\,\mathrm{L_{K,\odot}}$ per century. Assuming that one supernova releases $E_{\rm SN\,Ia} = 10^{51}$ erg into the interstellar medium, we obtain about $1.5 \times 10^{40}\,\mathrm{erg\,s^{-1}}$ energy that goes into the ISM. The minimal energy required to lift the gas in the gravitational potential of the galaxy can be calculated from $E_{\rm lift} = 7.2\dot{M}_\star\sigma_\star^2$ (David et al. 2006). With $\sigma_\star = 156 \pm 23\,\mathrm{km\,s^{-1}}$ (Lawrie 1983), we obtain $\sim 3.3 \times 10^{39}\,\mathrm{erg\,s^{-1}}$. If the gas is heated to the observed temperature by supernovae, it requires $\sim 10^{39}\,\mathrm{erg\,s^{-1}}$. These estimates indicate that the energy input from supernovae is approximately three to four times larger than the minimal energy required to drive a galactic wind from the galaxy, similar to the result of David et al. (2006) for low-luminosity ellipticals.

Type Ia supernovae will also contribute to the chemical enrichment of the ISM with iron-peak elements. Typically, $0.7\,\mathrm{M_\odot}$ of iron is provided by each SN Ia event (Nomoto, Thielemann & Yokoi 1984; Shigeyama et al. 1992; Iwamoto et al. 1999), which gives about $3.4 \times 10^{-4}\,\mathrm{M_\odot}$ of iron per year. Assuming complete mixing of the supernova ejecta with the stellar wind material, we would expect the iron abundance in the hot ISM $\approx 1.1 \times 10^{-2}$ by mass, which exceeds the solar value of 1.9×10^{-3} (Anders & Grevesse 1989) by a factor of ∼6. The observed spectra are inconsistent with high iron abundance in simple one- or two-component thermal models, but these models cannot adequately describe the spectra anyway; therefore, this result cannot be used as a conclusive argument. On the other hand, the discrepancy between the high predicted and low observed abundance of iron is a well-known problem for elliptical galaxies, where Type Ia supernovae also play an important role in thermal and chemical evolution of the ISM; it has been addressed in a number of studies, e.g. Brighenti & Mathews (2005). We also note that although the iron is the primary element by mass in the Type Ia supernovae ejecta, the ISM will also be enriched by other elements, most significantly by nickel. The detailed analysis of this problem is beyond the scope of the present paper.

Assuming that the gas leaves the galaxy in a steady-state wind along the axis perpendicular to the plane of the disc, the outflow speed $v_{\rm w}$ can be calculated from $\dot{M}_\star = \pi r^2 \rho_{\rm gas} v_{\rm w}$ where $\rho_{\rm gas}$ is the average gas density estimated above and r is the radius of the base of the imaginary cylinder filled with the outflowing gas. This calculation gives $v_{\rm w} \sim 60\,\mathrm{km\,s^{-1}}$ which is smaller by a factor of a few than the local sound speed. Such a slow subsonic motion of the gas cannot explain the observed elongated shape of the gas distribution, which may be related to the magnetic fields and galactic rotation. We can use the fact that the shadow from the 10-kpc star-forming ring is present to estimate the extent of the gas along the axis perpendicular to the galactic disc. The angular distance of the shadow from the centre is ∼600–700 arcsec, giving the 'vertical' extent of the gas of $\gtrsim 2.5$ kpc.

4.3 Spiral arms

The ∼10 times higher X-ray to *K*-band ratios observed in the spiral arms (Table 4) and their different emission spectrum (Fig. 6) suggest that X-ray emission from spiral arms has a different nature from the bulge. As spiral arms are associated with star formation, an

obvious candidate is X-ray emission from young stellar objects (protostars and pre-main-sequence stars) and young stars, which are well-known sources of X-ray radiation (Koyama et al. 1996; Carkner, Kozak & Feigelson 1998; Giardino et al. 2007).

As X-ray emission from the spiral arms is associated with young objects, it is natural to characterize it with the L_X/SFR (star formation rate) ratio. We compute this ratio for the regions used in spectral analysis. The FIR flux was determined from the 160 μm *Spitzer* image, 290 Jy. In computing this value, we subtracted the blank-sky background of nearby fields. To convert it to SFR, we used results of IR spectral fits from Gordon et al. (2006), which gave SFR = $9.5 \times 10^{-5} F_{160\,\mu}/\mathrm{Jy}\,\mathrm{M}_\odot\,\mathrm{yr}^{-1}$ for the M31 distance. Thus, we obtained the SFR of $0.028\,\mathrm{M}_\odot\,\mathrm{yr}^{-1}$ in the region used for the analysis. The X-ray luminosity in the same region is $3 \times 10^{37}\,\mathrm{erg\,s}^{-1}$ in the 2–10 keV band. After subtracting the X-ray emission due to the old stellar population, we obtain $2.6 \times 10^{37}\,\mathrm{erg\,s}^{-1}$ energy. From this, we can compute $L_X/\mathrm{SFR} \approx 9.4 \times 10^{38}\,\mathrm{erg\,s}^{-1}\,(\mathrm{M}_\odot\,\mathrm{yr}^{-1})^{-1}$. This value is ∼1/3 of the total L_X/SFR arising from high-mass X-ray binaries which is $2.5 \times 10^{39}\,\mathrm{erg\,s}^{-1}\,(\mathrm{M}_\odot\,\mathrm{yr}^{-1})^{-1}$ (Grimm et al. 2003; Shtykovskiy & Gilfanov 2005).

5 CONCLUSIONS

We investigated the origin of unresolved X-ray emission from M31 using *Chandra* and *XMM–Newton* data. We demonstrated that it consists of three different components.

(i) Broad-band emission associated with the old population, similar to the Galactic ridge emission in the Milky Way. It is a combined emission of a large number of weak unresolved sources of stellar type, the main contribution being from cataclysmic variables and active binaries. The surface brightness distribution of this component approximately follows the distribution of *K*-band light. The absorption-corrected X-ray to *K*-band luminosity ratios are compatible with the Milky Way values. The total luminosity of this component inside the central $800 \times 400\,\mathrm{arcsec}^2$ is of the order of $\sim 3 \times 10^{38}\,\mathrm{erg\,s}^{-1}$ in the 0.5–10 keV band.

(ii) Soft emission localized in the inner bulge of the galaxy along its minor axis. This emission is from ionized gas with a temperature of the order of ∼300 eV, although its spectrum cannot be adequately described by a simple one- or two-temperature model of optically thin emission from a gas in a collisional ionization equilibrium. The 0.5–2 keV luminosity in the central $8 \times 20\,\mathrm{arcmin}^2$ area is $\sim 2 \times 10^{38}\,\mathrm{erg\,s}^{-1}$ and the absorption-corrected bolometric luminosity is $\sim 5 \times 10^{38}\,\mathrm{erg\,s}^{-1}$. The total mass of the gas is $\sim 2 \times 10^6\,\mathrm{M}_\odot$ and its cooling time is ∼250 Myr. The surface brightness distribution is drastically different from the stellar light distribution, and it is significantly elongated along the minor axis of the galaxy. The morphology of the soft emission suggests that gas outflows along the direction perpendicular to the galactic plane. The mass and energy budget are maintained by the mass loss by the evolved stars and Type Ia supernovae. The 'vertical' extent of the gas exceeds $\gtrsim$2.5 kpc. These results are in good agreement with those recently obtained by Li & Wang (2007).

(iii) Hard emission from spiral arms. In the 0.5–7 keV band this emission has approximate power-law shape with $\Gamma \approx 2$. It is most likely associated with star-forming regions and is due to young stellar objects and young stars. The $L_X/\mathrm{SFR} \approx 9.4 \times 10^{38}\,\mathrm{erg\,s}^{-1}\,(\mathrm{M}_\odot\,\mathrm{yr}^{-1})^{-1}$ which is about ∼1/3 of the contribution of high-mass X-ray binaries.

ACKNOWLEDGMENTS

We thank the anonymous referee for his/her useful and constructive comments. This research has made use of *Chandra* archival data provided by the *Chandra* X-ray Centre. *XMM–Newton* is an ESA science mission with instruments and contributions directly funded by ESA Member States and the USA (NASA). This publication makes use of data products from Two-Micron All Sky Survey, which is a joint project of the University of Massachusetts and the Infrared Processing and Analysis Center/California Institute of Technology, funded by the National Aeronautics and Space Administration and the National Science Foundation. The *Spitzer* Space telescope is operated by the Jet Propulsion Laboratory, California Institute of Technology, under contract with the National Aeronautics and Space Administration.

REFERENCES

Anders E., Grevesse N., 1989, Geochim. Cosmochim. Acta, 53, 197
Baldi A., Raymond J. C., Fabbiano G., Zezas A., Rots A. H., Schweizer F., King A. R., Ponman T. J., 2006, ApJ, 636, 158
Bell E. F., de Jong R. S., 2001, ApJ, 550, 212
Borozdin K. N., Priedhorsky W. C., 2000, ApJ, 542, L13
Brighenti F., Mathews W. G., 2005, ApJ, 630, 864
Carkner L., Kozak J. A., Feigelson E. D., 1998, AJ, 116, 1933
David L. P., Forman W., Jones C., 1990, ApJ, 359, 29
David L. P., Jones C., Forman W., Vargas I. M., Nulsen P., 2006, ApJ, 653, 207
Dickey J. M., Lockman F. J., 1990, ARA&A, 28, 215
Dwek E. et al., 1995, ApJ, 445, 716
Fabbiano G., 2006, ARA&A, 44, 323
Fabbiano G., Trinchieri G., van Speybroeck L. S., 1987, ApJ, 316, 127
Fleming T. A., Molendi S., Maccacaro T., Wolter A., 1995, ApJS, 99, 701
Giardino G., Favata F., Micela G., Sciortino S., Winston E., 2007, A&A, 463, 275
Gilfanov M., 2004, MNRAS, 349, 146
Gordon K. D. et al., 2006, ApJ, 638, L87
Grimm H.-J., Gilfanov M., Sunyaev R., 2003, MNRAS, 339, 793
Henderson A. P., 1979, A&A, 75, 311
Hickox R. C., Markevitch M., 2006, ApJ, 645, 95
Irwin J. A., Bregman J. N., 1999, ApJ, 527, 125
Iwamoto K., Brachwitz F., Nomoto K., Kishimoto N., Umeda H., Hix W. R., Thielemann F.-K., 1999, ApJS, 125, 439
Jarrett T. H., Chester T., Cutri R., Schneider S. E., Huchra J. P., 2003, AJ, 125, 525
Kent S. M., 1992, ApJ, 387, 181
Kim D.-W., Fabbiano G., 2003, ApJ, 586, 826
Knapp G. R., Gunn J. E., Wynn-Williams C. G., 1992, ApJ, 399, 76
Koyama K., Hamaguchi K., Ueno S., Kobayashi N., Feigelson E. D., 1996, PASJ, 48, 87
Lawrie D. G., 1983, ApJ, 273, 562
Li Z., Wang Q. D., 2007, ApJ, 668, L39
Macri L. M. et al., 2001, ApJ, 549, 721
Mannucci F., Della Valle M., Panagia N., Cappellaro E., Cresci G., Maiolino R., Petrosian A., Turatto M., 2005, A&A, 433, 807
Moretti A., Campana S., Lazzati D., Tagliaferri G., 2003, ApJ, 588, 696
Nevalainen J., Markevitch M., Lumb D., 2005, ApJ, 629, 172
Nieten C., Neininger N., Guelin M., Ungerechts H., Lucas R., Berkhuijsen E. M., Beck R., Wielebinski R., 2006, A&A, 453, 459
Nomoto K., Thielemann F.-K., Yokoi K., 1984, ApJ, 286, 644
Primini F. A., Forman W., Jones C., 1993, ApJ, 410, 615
Revnivtsev M., Sazonov S., Gilfanov M., Churazov E., Sunyaev R., 2006, A&A, 452, 169
Revnivtsev M., Churazov E., Sazonov S., Forman W., Jones C., 2007, A&A, 473, 783

Rieke G. H. et al., 2004, ApJS, 154, 25
Sazonov S., Revnivtsev M., Gilfanov M., Churazov E., Sunyaev R., 2006, A&A, 450, 117
Shigeyama T., Nomoto K., Yamaoka H., Thielemann F.-K., 1992, ApJ, 386, L13
Shirey R. et al., 2001, A&A, 365, L195
Shtykovskiy P., Gilfanov M., 2005, A&A, 431, 597
Simien F., Athanassoula E., Pellet A., Monnet G., Maucherat A., Courtes G., 1978, A&A, 67, 73
Stanek K. Z., Garnavich P. M., 1998, ApJ, 503, 131
Stephens A. W. et al., 2003, AJ, 125, 2473
Strüder L. et al., 2001, A&A, 365, L18
Supper R., Hasinger G., Pietsch W., Truemper J., Jain A., Magnier E. A., Lewin W. H. G., van Paradijs J., 1997, A&A, 317, 328
Takahashi H., Okada Y., Kokubun M., Makishima K., 2004, ApJ, 615, 242
Trinchieri G., Fabbiano G., 1991, ApJ, 382, 82
Turner M. J. L. et al., 2001, A&A, 365, L27
van Speybroeck L., Epstein A., Forman W., Giacconi R., Jones C., Liller W., Smarr L., 1979, ApJ, 234, 45
Voss R., Gilfanov M., 2007, A&A, 468, 49
Walterbos R. A. M., Kennicutt R. C., 1987, A&AS, 69, 311
Walterbos R. A. M., Kennicutt R. C., 1988, A&A, 198, 61
West R. G., Barber C. R., Folgheraiter E. L., 1997, MNRAS, 287, 10

This paper has been typeset from a TEX/LATEX file prepared by the author.